Measurement Science and Technology

PAPER • OPEN ACCESS

A highly sensitive laser focus positioning method with sub-micrometre accuracy using coherent Fourier scatterometry

To cite this article: Dmytro Kolenov *et al* 2020 *Meas. Sci. Technol.* **31** 064007

View the article online for updates and enhancements.

You may also like

- Hybrid metrology for nanometric energy harvesting devices
Lauryna Siaudinyte, P-E Hansen, R Koops et al.

- An insight into optical metrology in manufacturing
Yuki Shimizu, Liang-Chia Chen, Dae Wook Kim et al.

- Interferometric coherent Fourier scatterometry: a method for obtaining high sensitivity in the optical inverse-grating problem
S Roy, N Kumar, S F Pereira et al.

This content was downloaded from IP address 202.8.112.224 on 05/07/2023 at 08:25

IOP Publishing

Measurement Science and Technology

Meas. Sci. Technol. **31** (2020) 064007 (9pp)

https://doi.org/10.1088/1361-6501/ab7063

A highly sensitive laser focus positioning method with sub-micrometre accuracy using coherent Fourier scatterometry

Dmytro Kolenov, Peiwen Meng and Silvania Pereira

Optics Research Group, Imaging Physics Department, Faculty of Applied Sciences, Delft University of Technology, Lorentzweg 1, 2628 CJ Delft, The Netherlands

E-mail: d.kolenov@tudelft.nl

Received 15 November 2019, revised 22 January 2020
Accepted for publication 27 January 2020
Published 3 April 2020

Abstract

We report a novel method of focus determination with high sensitivity and submicrometre accuracy. The technique relies on the asymmetry in the scattered far field from a nanosphere located at the surface of interest. The out-of-focus displacement of the probing beam manifests itself in imbalance of the signal of the differential detector located at the far field. Up–down scanning of the focussed field renders an error *S*-curve with a linear region that is slightly bigger than the corresponding vectorial Rayleigh range. We experimentally show that the focus can be determined not only for a surface with high optical contrast, such as a silicon wafer, but also for a weakly reflecting surface, such as fused silica glass. Further, for the probing wavelength of 405 nm, three sizes of polystyrene latex spheres, namely 200, 100, and 50 nm in diameter, are tested. Higher sensitivity was obtained as the sphere diameter became smaller. However, due to the fact that the scattering cross-section decreases as the sixth power of the nanosphere diameter, we envision that further size reduction of the studied sphere would not contribute to a drastic improvement in sensitivity. We believe that the proposed method can find applications in bio/nano detection, micromachining, and optical disk applications.

Keywords: focus determination, sensitive method, nanoparticle at surface, coherent Fourier scatterometry

(Some figures may appear in colour only in the online journal)

1. Introduction

Focussed light plays a vital role in modern technology in the fields of optical lithography, micro-machining, optical data storage, nanostructure characterisation, and biology [1, 2]. The inability to define and maintain the focal plane position on the sample or surface results in degradation of resolution [3], non-optimal energy use of the focussed field [4], damage of the sample [5], failure to store data [6, 7], uncertainty in the localisation of cells, and lack of reproducibility of biological results [8, 9].

Nowadays, one can also find imaging techniques dedicated to the detection of deepsubwavelength nanoparticles on top of a surface, with sizes that can be smaller than 10 nm (for example, gold nanoparticles in optical detection using interferometric schemes [10]). Robust visualisation and discrimination of the deepsubwavelength particles are also possible with techniques such as label-free interference reflectance imaging of IRIS or ISCAT [11]. In addition to excellent focussing, the smoothness and flatness of the substrate

Original content from this work may be used under the terms of the Creative Commons Attribution 4.0 licence. Any further distribution of this work must maintain attribution to the author(s) and the title of the work, journal citation and DOI.

 © 2020 The Author(s). Published by IOP Publishing Ltd Printed in the UK

is crucial [12, 13]. Interference techniques allow for high spatio-temporal resolution; however, they suffer from potential defects in lenses, readout and shot noise in the camera, and mechanical instability. Advanced post-processing algorithms can compensate for the resultant degradation of image quality and the drop in the magnitude of the weakly scattered signals [14].

Aside from extracting information about the sample using conventional measurands such as amplitude and phase information, by using high-numerical aperture (NA) objective lenses, optically induced forces can be exerted on the illuminated object. In this scenario, the resolution limit becomes irrelevant, and instead the signal-to-noise ratio (SNR) is essential. For example, the technique of optical pseudoelectrodynamics microscopy (OPEM), operating in the robust through-focus regime, reconstructs quantities such that 'pseudo-mechanical' work and its transverse gradient 'pseudo-force' can lead to a higher SNR and sensing of sub-10 nm features in semiconductor nanopatterns [15].

While the problem of determining the focus position in an accurate way is essential for many applications such as those mentioned above, there is no single general solution, and in the literature one finds various techniques that are applied depending on the limitations and other conditions of the experimental set-up. These limitations might include sensitivity to vibrations and shocks, the ability to work on the fly, scan speed, ease of use, etc.

For coherent sources of illumination, monochromatic confocal systems are commonly used to measure the surface position or to simply define the focus position [5, 16]. In a confocal system, the light is focussed on the object plane and this plane is imaged on the point detector (usually an optical fibre) or a pinhole. The image is obtained by scanning the spot or the sample in the lateral direction, i.e. perpendicular to the optical axis. Coherent Fourier scatterometry (CFS) is an optical technique that is similar to confocal systems but instead of imaging the object plane on the point detector, the back focal plane is imaged using a charge-coupled device (CCD) camera [17]. In this way, the light scattered from the object and reflected from the surface is coherently added in the far field. The resulting Fourier plane is a collection of electric field contributions along the angles that belong to the back focal plane of the objective. If the full far field is recorded at a CCD, each pixel will correspond to one scattered angle within the NA of the objective. In the case of a sample containing isolated nanoparticles, it has been observed that the far-field intensity distribution changes as the nanoparticle passes through the focussed beam. Using a split detector instead of a CCD camera, the asymmetry in the far field that occurs when the relative position of the nanoparticle and the focussed beam changes, has led to successful detection of subwavelength particles [18]. The combination of speed, low power of illumination, and robustness makes this technique an outstanding scientific tool for surface contamination inspection, and potentially for biological applications.

This article proposes a novel sensitive focus-finding method based on the detection of subwavelength particles on surfaces using CFS. As a spin-off of the method, the position of the surface under the particle can be determined with submicrometer accuracy in a non-contact manner. With the aid of differential signal readout, we can sensitively localise the position of the nanoparticle both in the horizontal and vertical planes. While the idea of detecting the focus position on the surface with the aid of differential detection is not new [6, 19], to the author's best knowledge, exploiting an isolated particle at the surface to find the surface position has never been proposed previously. Experimentally, the presented focus-finding technique allows one to generate the error S-curve with a linear region that is a few times higher than the corresponding vectorial Rayleigh range $S \approx 3.8Z_r$ for the case of a polystyrene latex (PSL) nanoparticle 50 nm in diameter deposited on a silicon wafer and a linear region of $S \approx 5.6Z_r$ for a glass substrate containing a 100 nm PSL nanoparticle. Furthermore, three sizes of PSL nanoparticles 200, 100, and 50 nm in diameter, were tested, and it was observed that the increase in sensitivity was inversely proportional to the particle size.

The remainder of the article is organised into the following sections: in section 2, we describe the measurement approach, and discuss the position-dependent phase and the procedure we used for the uncertainty estimation. In section 3, we present the experimental results. In section 4, we discuss the limitations of the technique and present the conclusions4, followed by the appendix.

2. Methods

2.1. Measurement approach

In CFS, the position and size of the nanoparticle can be obtained from a raster scanning procedure over the surface of interest. Given that coherent light is used, the physical quantity that is measured directly at the far field is an interference between the scattered field from the particle and the reflected field from the surface. The general layout of the scatterometer, particularly suitable for the detection of deep subwavelength particles, is shown in figure 1(A).

When the sample on the piezo stage is scanned in a raster fashion (line scan along the X axis with a step in the Y axis between the lines), the scattering from a single isolated particle contributes to the differential signal of the split detector (L–R) over multiple scanning lines (signal group) as shown schematically in figure 1(B). The full area of the scan map is $A = X \times Y$ (μm^2), where X and Y are chosen to be a few times larger than the size of the scanning spot. Importantly, a step displacement Δy of the stage along Y the direction should be a couple of times smaller than the diameter of the sphere. The orthogonal direction, where the sampling of the signal should be high to give a valid representation in the time span, defines the width of the scan in the X direction. If there is only one of such group of signals in the scanned area A, we can assume that the particle is isolated. Within one scanning map, the Y_{centre} position is defined when the signal group amplitude is maximum, and the X_{centre} position is attributed to the zero-crossing of the corresponding particle profile (figures 1(B) and (C)).

The working principle of the focus determination system is described via the flowchart in figure 2(A). First, the downward

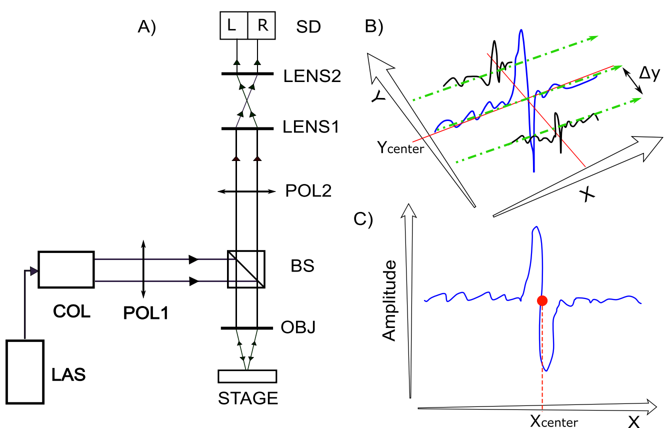

Figure 1. (A) Scheme of the experimental set-up. LAS: blue 405 nm laser diode; COL: collimator; POL1, POL2: linear polarisers; BS: beam splitter; OBJ: microscope objective NA = 0.9; STAGE: piezo-controlled stage (*XYZ*); LENS1, LENS2: telescopic lens system; SD: split detector. (B) Scheme showing the raster scanning of the substrate containing one isolated nanoparticle. The scan is line per line, along the *X* direction. (C) Differential signal of a single scanning line along *X* through the spherical particle. The zero signal refers to the centre of the particle

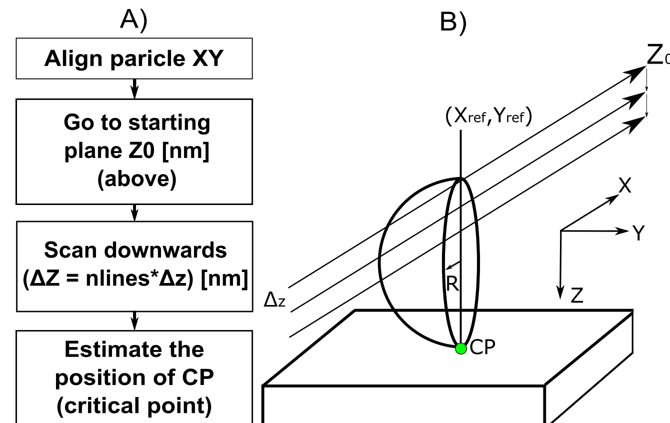

Figure 2. (A) Flowchart of the proposed focus-finding method. A schematic drawing of the scanning procedure. (B) The focussed spot moves to positive *Z* as the piezo stage steps in the opposite direction. For each position along *Z*, a line scan is performed along *X*. The plane *XZ* is at the middle of the sphere of radius *R*.

scanning axis *Z* needs to be aligned with 'centre' of the particle. The coordinate pairs in the *XY* plane referring to the centre of the particle in the lateral direction are obtained by averaging the coordinate *XY* in all *Z* planes that correspond to zero intensity at the detector in (see figure 1(C)), i.e. $(X_{\mathrm{ref}}, Y_{\mathrm{ref}}) = \left(\overline{X_{\mathrm{centre}}}, \overline{Y_{\mathrm{centre}}}\right)_{Zj}$. The next two steps are as follows: (i) move in the longitudinal direction to a plane above the particle defined as Z_0 and (ii) perform single line scans in the *X* direction around the point for different values of *Z*. Collecting only one profile at a time allows us to keep the method time-efficient. The stage moves downwards a predetermined amount of lines n_{lines}, which has to be big enough to go through the optimal focus. In our experiment, the steps in the *Z* direction were $\Delta z = 5$ nm, rendering the complete through-focus distance $\Delta Z = n_{\mathrm{lines}} \times \Delta z$. A schematic of this procedure is shown in figure 2(B). Essentially, the scanning is performed in a raster fashion, but now in the plane *XZ*. The obtained differential signal for each scan line is zero when the particle is centreed w.r.t. the focussed spot and is positive or negative when the particle is either on the left or on the right of the focussed spot along the *X* axis. It has also been observed that the relative intensity of the differential signal corresponding to the left or right side changes with the chosen *Z* plane. At one particular *Z* plane, the maximum intensities of the differential signal for *X* positions located on the left and on the right of the centre of the particle are balanced (the same intensity, opposite signal), defined as the (critical point (CP) in figure 2(B). At other *Z* planes, the maximum left/right intensities are different, i.e. the signal is unbalanced. The distance from the initial plane to the position of the CP can be computed by adding the initial position with the distance to the critical point and including the error. In figure 3(A) we show these situations schematically (see signals on the three squares) as a function of the defocus position. Also in figure 3(A), we show that if we plot the imbalance between the right and left maximum intensities,

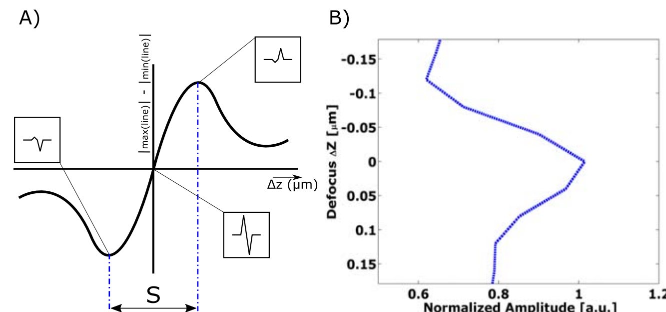

Figure 3. (A) The measure of imbalance of the lateral scan line as a function of the defocussing delta *Z*. *S*-curve for the through-focus error signal. (B) The maximum in the amplitude of the simulated through-differential signal occurs when the focus is located under the spherical particle, i.e. defocus $\Delta Z = 0$.

defined as $|I_{\mathrm{max}}| - |I_{\mathrm{min}}|$ as a function of the *Z* displacement, one obtains an *S*-curve.

This focus error signal changes from its maximum negative to its maximum positive value over a distance that is typically a few vectorial Rayleigh ranges and the slope depends inversely on the diameter of the particle.

The far-field nanoparticle scattering is simulated for the defocus distance of two Rayleigh ranges ≈ 360 nm and for a linearly polarised focussed spot. In figure 3(B), the maximum in the modulus of the amplitude of the differential signal that is obtained for each *X* scan at one fixed defocus position is plotted against the defocus position. In the plot, zero defocus means that the focal plane is set at the interface (air/substrate). As can be seen in the figure, the maximum amplitude of the differential signal occurs when the focal plane is set at the interface, i.e. under the particle. This result suggests that the zero crossing of the *S*-curve is not only a position to keep the instrument in-focus for nanoparticle detection, but also the location of the surface under test in the *Z* direction. We also observed that the smaller the particles are, the steeper is the slope of the *S*-curve. More details about the simulations that led to the result in figure 3(B) are given in the next section.

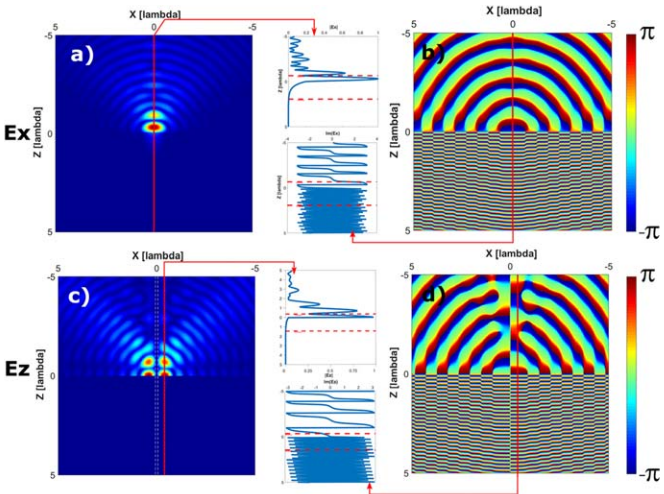

Figure 4. Simulated amplitude and phase distributions of the focussed field in the XZ plane. The middle part of each panel represents the cross-section of either amplitude or phase (red arrows) and dashed lines represent the minima of amplitude. The absolute values of the amplitude E_x is given in (a) and E_z in (c), and the corresponding phases in (b) and (d). The $NA = 0.9$, the wavelength $\lambda = 405$ nm, and the interface is between air ($z < 0$) and silicon ($z > 0$).

2.2. Position-dependent phase

In order to understand the influence of the focus position in the nanoparticle/interface scattering, we have performed rigorous 3D vectorial simulations. In the first set, we calculated the focussed field without a nanoparticle on a interface using the Richards and Wolf integrals. The implementation of these calculations is explained in detail in [20]. The results shown in figure 4 are calculated for a linearly polarised (along the X axis) uniform amplitude focussed field, where in the left colunm we plot the modulus of the amplitude of the $|(E_x(z)|$ and the $|(E_z(z)|$ components and in the right column their corresponding phases as a function of $-5\lambda \leq z \leq 5\lambda$. The numerical aperture $\mathrm{NA} = 0.9$ and the wavelength $\lambda = 405$ nm. The interface is between air ($z < 0$) and silicon ($z > 0$) and the focal plane is set at the interface (Z = 0). Notice that in the case of the x-linearly polarised focussed spot, the E_y component is not shown since this is negligible. To determine the phase change, first we estimate the on-axis (Z) positions of the first two minima close to the interface in the amplitude of the focussed field components. Second, we compute the phase difference between the minima based on the corresponding phase slices. For the E_x component, we estimate that the π phase difference occurs over the distance $\Delta Z = 1.049$ µm and for the E_z component $\Delta Z = 0.73$ µm. This phase change suggests that when the particle on the silicon surface is moved along the Z direction, the collected signal will have the reverse polarity over a certain vertical distance. It is important to note that we only show the slices of the phase map in the direction normal to the interface. The far-field result of the near-field focussed spot interaction is more complicated and accounts for every angular direction within the NA.

The far-field differential signal plotted as a function of the scan position along the X axis presents asymmetric side lobes

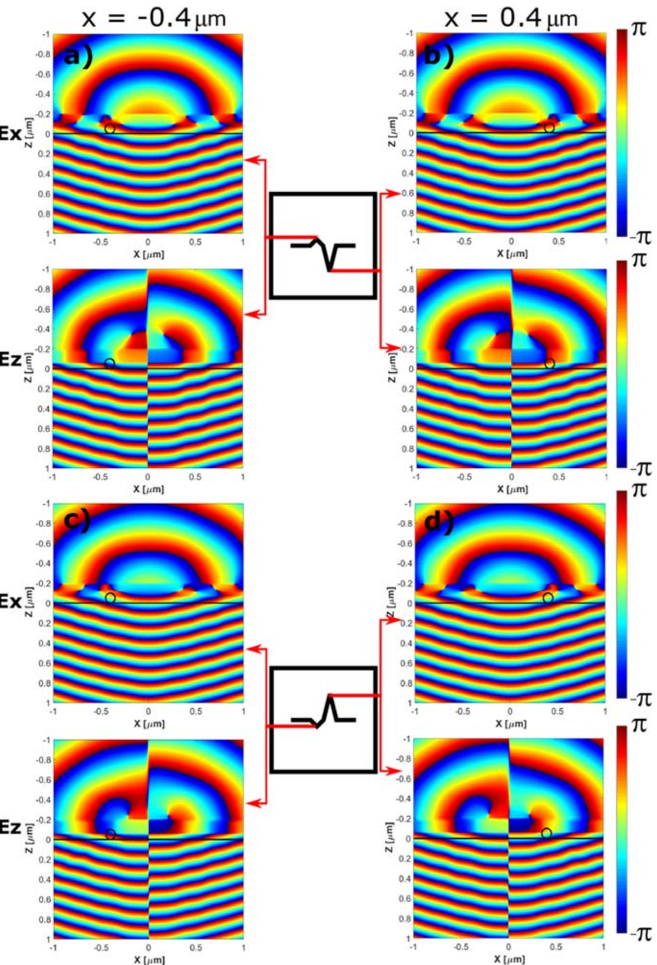

Figure 5. The phase distributions in the XZ plane of a 100 nm PSL particle on top of silicon. The particle is moved in the X direction through the focussed beam centred at $X = 0$. In the upper panels (a) and (b) the focal plane is set at $z = -0.11$ µm. in the lower panels (c) and (d) the focal plane is set inside the slab at $z = 0.11$ µm. The particle in the X axis is positioned at $x = -0.4$ µm in (a) and (c), and $x = 0.4$ µm in (b) and (d). The red arrows between the diagrams indicate the corresponding position on the signal of the X axis scan.

(as shown earlier in figure 3) as we set the focal plane at different Z positions with respect to the interface. We believe that this imbalance is due to the position-dependent phase of the focussed field. For comparison, we consider two situations: first, we set the focal plane right above a 100 nm PSL particle, i.e. at $z = -0.11$ µm, as shown in figures 5 (a) and (b), and second, the focal plane is set inside the silicon slab at $z = +0.11$ µm in (c) and (d). Further, we show the total near field for the E_x and E_z components if the nanoparticle is displaced in the X axis by –0.4 µm (left column) or +0.4 µm w.r.t. the centre of the beam, which is located at $X = 0$. Here, the numerical analysis is based on the FDTD method using Lumerical, which allows simulating a spherical particle on a surface, illuminated with a focussed beam. As the incident field, we use the focal spot with the linear polarisation that is obtained with the CZT method [21]. It is instructive to study the near-field phase distribution for two extrema of the simulated differential signals.

Table 1. Expanded uncertainty contributions for computing the surface position.

PSL diameter (nm)	$2 \times U_{\text{partc}}$ (µm)	$2 \times U_{\text{posc}}$ (µm)
	Silicon surface	
200	±0.7392	±0.8110
100	±0.2301	±0.2494
50	±0.0864	±0.0936
	Glass surface	
200	±1.007	±1.1833
100	±0.3067	±0.3374

The opposite (at $x = -0.4$ µm and $x = 0.4$ µm) phase components for the x component angle(E_x) for the two extrema look similar, also for both focus positions. The angle(E_z) component, in contrast, changes both in magnitude and spatial distribution. We can conclude that, specifically, the phase changes in the Z component of the incident field are responsible for the scattering from the symmetric object producing the unbalanced amplitude at the far field. For simulations of a non-spherical scattering object, please see appendix B.

2.3. Uncertainty estimation

We put together the uncertainty contributions according to the following equation for the combined standard uncertainty (see further details in appendix A): where $\sigma_y, \sigma_{s_z}, \sigma_{s_z}, R_{yz}$ denote standard deviations of the Y coordinate (fluctuation versus the reference Y_{ref}), Z coordinate (fluctuations of zero in the Ss-curve), intrinsic Z error of the piezo, and cross-correlation between the horizontal and vertical movement, respectively. In addition to the standard uncertainties reported with the partial correlation U_{partc} between the Y and Z contributions, we include more conservative estimates assuming the full (positive) correlation [22]. Finally, to establish a more reasonable accuracy of the technique, we use the expanded uncertainty U given by $U = k \times U_{\text{partc/posc}}$, where k is the coverage factor and $U_{\text{partc/posc}}$ is the combined standard uncertainty. We take the value of the coverage factor to be $k = 2$, which is equivalent to approximately 95% coverage for a normal distribution. Importantly, to collect the data, we have used two settings of optical power: the peak power at the objective (before being focussed on the substrate) is either $P_{\text{low}} = 0.58$ mW or $P_{\text{high}} = 1.64$ mW. For the cases of 200 and 100 nm PSL particles on silicon and 200 nm PSL particles on glass, we have used the power P_{low}, while for the 50 nm PSL particles on silicon and 100 nm PSL particles on glass, we have used P_{high}. For most of the demonstrated cases, at wavelength of $\lambda = 405$ nm, we estimate sub-micrometer accuracy in finding the position of the surface (table 1). The exception is the 200 nm PSL particle on top of the glass surface, where the uncertainty is slightly above 1 µm. It is thus not recommended to use such a large diameter for focus-searching purposes with materials of low reflection. The obtained results are comparable to those of the focus searching methods used in micro-machining applications such as that based on a nonlinear harmonic generation [23]:

$$U_{partc} = \sqrt{\sigma_y^2 + \sigma_{s_z}^2 + 2R_{yz}\sigma_y\sigma_z + \sigma_{s_z}^2}, \quad (1)$$

$$Z_{\text{r}} = \lambda/4[1 - \cos(\alpha)]. \quad (2)$$

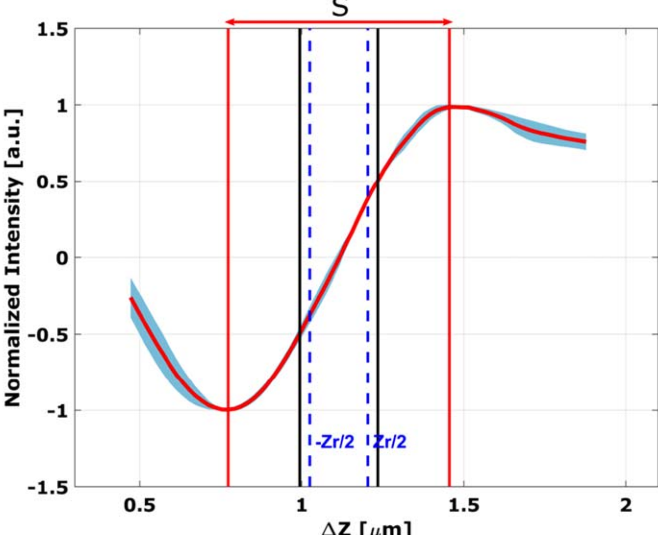

Figure 6. Measured mean S-curve of the through-focus scan of a (nominal) 46 nm PSL sphere on top of a silicon wafer (red curve). The sky blue color indicates one standard deviation with respect to the mean over four data sets. Black vertical lines define the region with 50% Pk–Pk of the curve lies and the red vertical lines show the region over which the slope S is estimated compared to the Rayleigh range one (blue dashed lines). For this data, the slope $S \approx 3.8Z_r$.

Table 2. Comparison between 200, 100, and 50 nm PSL nanoparticles studied in the through-focus measurements. The middle 100% of the S-curve for each measurement falls within S (µm).

PSL diameter (nm)	The linear region the of S-curve $S \pm \sigma$ at 100% Pk–Pk (µm)	
	Silicon surface	Glass surface
200	1.1618 ± 0.0167	1.2817 ± 0.0429
100	0.8016 ± 0.0104	1.0116 ± 0.0033
50	0.68273 ± 0.0088	

3. Results

Figure 6 shows the S-curve obtained from the through-focus signal for a sample of monodisperse polystyrene calibrated spheres (PSL) that have been spin coated on top of a silicon wafer. For this plot, the scanning with the focussed spot is done through an isolated sphere of nominal diameter $d = 46 \pm 2$ nm. For the acquired S-curve, 100% (peak-to-peak (Pk–Pk)) of the slope lies within $S \approx 3.8Z_{\text{r}}$, where Z_{r} is the Rayleigh range calculated from the vectorial diffraction theory according to the formula $Z_{\text{r}} = \lambda/4[1 - \cos(\alpha)]$, where $\alpha = a\sin(\text{NA})$. Note

Table 3. Sensitivity comparison ratio $G = T'/T$ of the presented method to various implementations of the known astigmatism method. T', T are the ratio of the linear region of each S-curve to the corresponding Rayleigh range for each implementation. The reference T used for the comparison is the value obtained in this paper for a 50 nm particle, which is $T = 3.8Z_r$.

Linear region S-curve S (µm)	Details	Rayleigh range Z_r' (nm)	Ratio $T' = S/Z_r'$	Ratio $G = T'/T$	Reference
6	$\lambda = 633$ nm, NA = 0.6	791.25	7.6	2	[24]
4	$\lambda = 405$ nm, NA = 0.65	421.7	9.48	2.5	[25]
3	$\lambda = 405$ nm, NA = 0.85	214	14.02	3.67	[26]
2	$\lambda = 405$ nm, NA = 0.85		9.34	2.45	[27]

that this Rayleigh range is almost three times smaller than the paraxial one [28]. Notice how the middle 50% of the curve is slightly largerthan the Rayleigh range. Remarkably, in the right half of the S-curve, the region after its maximum positive value decreases more slowly than the corresponding region in the left half of the S-curve. The most likely explanation for this result is the scattering from the background that increases the balance in the collected signal as we scan below the focus, deeper under the particle. Further, we investigate the effects of the particle diameter on the sensitivity of the acquired S-curve (see table 2). The motivation for this is to show that the method is compatible with several particle sizes as it is not always possible to add a particle with a known size. Second, as our prototype includes custom-made electronics for the detector, which allows us to detect particles < 80 nm (low dark noise and with a design to minimise pick-up from the environment), in contrast when using an off-the-shelf photodetector, there will be considerably more noise and it will be difficult to detect small scattering signals from spheres < 100 nm in diameter. In this case, slightly larger particles could be used.

For the sensitivity comparison, the S-curves were acquired for the same experimental conditions of sampling, scanning speed, and vertical and horizontal displacement steps. Each profile is based on the averaging of at least four data sets for each particle size. Evidently, the slope of the S-curve increases when smaller particles are studied. For a sphere of 50 nm diameter, as compared to other samples, for the variation of the linear region extent, as projected to the vertical axis $\Delta Z \pm \sigma$, the mean distance S is the smallest. The main reason is the shorter acquisition time needed to record multiple data sets for averaging, during which the whole system is less perturbed compared to longer scans for larger particles. Next, the decrease of the particle diameter does not linearly improve the sensitivity of the acquired curve. From the electromagnetic point of view, we are not dealing with physical objects but rather with a collection of emitting sources. The behaviour can be better understood from the perspective of scattering by a sphere on a substrate [29]. Functionally, the differential scattering cross section (DSCS) is proportional to the sixth power of particle size and this diameter dependency is more pronounced for a particle at the interface (by approximately eighth power [30].) Following a simple simulation of a horizontal dipole-like particle at the interface, the slope in the scattering response as a function of the particle size is fairly small for the particles in the domain $< \lambda/4$. At the same time, the change in slope is rather drastic for the larger particles $> \lambda/4$. Thus, in order to benefit from tiny particles in focus searching, the sensitivity of the detector should be suitable for recording small changes in the scattered intensity. In addition, we observed that the slope of the S-curve for a 50 nm particle is close to the slope of a 100 nm sphere . Thus, we expect that the sensitivity would not improve dramatically if < 50 nm particles were used. It follows from table 3 that the sensitivity of the proposed technique outperforms a set of results demonstrated by several implementations of one of the most commonly used techniques for focus control, namely, astigmatism. For the published results mentioned in table 3, the extents of the linear region S for the corresponding S-curves (first column) were taken directly from the original publication, while the corresponding Rayleigh ranges were computed by the authors of the current article. Since the benchmark results were based on systems with NA ≥ 0.6, the formula for the Rayleigh range was also computed according to the vector diffraction theory.

4. Discussion

This paper shows that high sensitivity in focus positioning can be achieved using the scattering from a nanoparticle on a surface. An immediate consequence is that the user might need to deposit a particle on the surface of interest, which may be unwanted. However, it is important to highlight that many application areas may not require depositing isolated spheres, but rather may use nanoparticles that are already be present in the sample. For example, in the domain of semiconductor manufacturing, the silicon wafers that come directly from the producer are not completely clean and do contain particles in the size domain from 30 to 100 nm. Additionally, during the lithography process, contamination is unavoidable [31]. If the assumption that the contamination has the shape of a sphere or an oblate spheroid can be made, the technique is directly applicable. In the case of biological samples, metal particles are sometimes present to stimulate resonance, so the smaller features of the neighbouring molecules or viruses become visible [32]. Further, in the fine maching stages of laser material processing, the surface will have low roughness but will locally have tiny scratches, pits, or dust [33]. All of these small isolated features could be used in our method.

We emphasise that in order for the technique to work, the particle diameter should be smaller than the depth of the focus of the given optical system. In our case, the DOF ≈ 360 nm whereas the maximum diameter of the studied particle was 200 nm. The DOF is defined as double the Rayleigh range DOF = $2Z_r$. On the other hand, the smallest suitable particle is defined by both the resolution of the vertical translation and the detection sensitivity of the technique itself. In order

to build up the error curve, the differential signal should be recorded at least at three vertical positions, when in practice one or two orders higher sampling is necessary. Further, the studied sphere, upon interacting with the focussed spot, should produce sufficient scattering to overcome the inherent experimental noise, specifically the noise floor at the detector. The strength of the collected signal, given a constant power of illumination and fixed particle diameter, depends both on the reflectivity of the sample and the material of the particle.

This technique could be extended to determine the tilt of a large surface such as a wafer by having a few nanoparticles distributed in the surface (spherical or elliptical), and determining the position of the surface at each point. In principle, to determine a two-dimensional tilt, three spheres distributed as a triangle would suffice.

5. Conclusions

In this paper, a novel sensitive method to find the focal plane of a laser beam that is focussed on a surface has been presented. The method is based on detecting the scattering in the far field of a nanoparticle that is deposited on a surface. We observed that the asymmetry in scattering from the nanoparticle that occurs when the focal plane is moved away from or towards the surface can be used to generate the *S*-curve error signal and consequently the position of the focal plane w.r.t. the reflecting surface. According to rigorous numerical simulations, we found that the zero in the *S*-curve occurs when the focal plane is set at the plane of the surface, i.e. directly under the nanoparticle. The obtained experimental results indicate that at best the linear region of the generated *S*-curve can be $S \approx 3.8 Z_r$ for a 50 nm PSL particle at the surface of a silicon wafer. Our method is also suitable for working with surfaces with low reflection, such as glass. The reflectivity of the surfaces, estimated for the most contributing angles within the NA, varies between 20% and 72% for glass and silicon, respectively. The generated *S*-curve for the case of a glass surface and a particle of 100 nm results in $S \approx 5.6 Z_r$. The achievable accuracy of the method is in the submicrometer range with a major contribution due to the translation stage (reported as the 2σ measurement uncertainty.) Moreover, several comparisons between the sensitivity of the presented method and various implementations of the astigmatism method for error-curve generation have been reported. We believe that the proposed method can find applications in microscopy, micro-machining, laser writing, optical lithography, and highly sensitive alignment systems.

Acknowledgments

Peiwen Meng acknowledges the Chinese Scholarship Council (CSC) and Dmytro Kolenov the High Tech Systems and Materials Research Program with Project No. 14660, financed by the Netherlands Organisation for Scientific Research (NWO), Applied and Technical Sciences division (TTW) for funding of this research.

Appendix A

A.1 Estimation of uncertainty

Complementary to section 2.3 we describe the method we have used to estimate the uncertainty in finding the position of the surface under the focussed spot with the nanoparticle as the mediator. The distance from the initial position, somewhere above the surface, to the final position, at the surface, is defined from the zero-crossing of the *S*-curve. The exact location of this point depends on multiple sources of measurement uncertainty. The process of calculating the uncertainty U includes two steps. First, we determine directly measured uncertainties and also take into account the uncertainties provided by manufacturers. Second, we combine those individual uncertainties in a root sum of squares. We use the type A evaluation process from GUM [34] to estimate the axial shifts along X, Y, and Z of the zero crossing position Z_{cp}. To find the 'centre' of the sphere, the maps over multiple vertical positions are acquired and the average reference position that corresponds to the maximum amplitude of the differential signal is stored. First, two uncertainties associated with this process are the standard deviations σ_x and σ_y of the X and Y coordinates, that describe the fluctuation versus the reference pair. σ_x makes no contribution to the final uncertainty as long as $\sigma_x < \Delta X/2$, where ΔX is the total width of the scan along X (a typical number is $\Delta X = 20$ µm.) Hence, for our method, the effect of misaligning the particle with respect to the focussed spot in the horizontal plane is described by σ_y. Deviation from the particle's true centre described by σ_y translates to the apparent vertical off-centre distance to the surface that is shorter than if it had been estimated exactly through the centre. Next, based on the repeated one line scan measurements along the Z axis line, from the resulting *S*-curve, σ_z can be estimated. For the final calculation of U, σ_z corresponding to the zero of curve Z_{cp} is used. Both σ_x and σ_y are calculated by averaging the $\left(\overline{X_{\mathrm{centre}}}, \overline{Y_{\mathrm{centre}}}\right)_{zj}$ coordinates of ten parallel signal maps across the total vertical distance of one micrometer, starting close to the focus position, with steps of 100 nm. The standard deviation σ_z is computed for the zero-crossing points of the *S*-curves by averaging four repeated profiles, each with a step of 5 nm between parallel scanning lines over distances that are different for different particle diameters, ranging from 1.5 µm to 2.6 µm. Following that, from the data sheet for the *Z*-translator stage (P-620.ZCD), we take the approximated accuracy error on the linearity of the Z displacement as double. For example, a 0.002% linearity for the full range of 50 µm is a 10 nm maximum deviation. Hence, the approximated accuracy error is 20 nm Pk–Pk or $\sigma_{s_z} = 0.02$ µm. In order to build up the error-curve profiles, the raw sampled data from the split detector are interpolated using Friedman's algorithm [35] with high coefficients of determination for all the studied particles diameters of 200, 100, and 50 nm $r_{yzmax} = max_{u,v \in \{i\} \times \{-n/2,\ldots,n/2\}} C\left(\overline{x,y}, u, v\right)$ and as.

Moreover, when a sample is fixed on top of a stack that is comprised of a *Z*-translator stage attached to an *XY*-translator stage, it is important to check the correlation between the axial contributions of uncertainty. We choose a digital image

correlation method [36, 37] applied to 2D CCD images of the reflected focussed spot at different axial positions, with these being close to the true focus. The core of the algorithm is to take two closely separated ($\Delta z = 5$ nm) images and take the cross-correlation between the subsets of corresponding numerical arrays. Next, one numerically introduces the pixel shifts and checks whether the correlation throughout pairs of subsets grows with respect to the non-shifted position. If this is the case, the vertical displacement of the wafer surface by Δz translates to the displacement Δy. The following equations demonstrate how we compute the final correlation coefficient R_{yz}, where I and I^{*} are intensity images at the CCD, separated by a vertical step of 5 nm. The subset size in our case is $n = 20$ pixels and the step between overlapping subsets is 10 pixels (the half-window of subset window size). Based on the two images of a large random defect > 5 μm in the silicon wafer, we estimate the cross-correlation between the Y and Z displacement as $R_{yz} = R_{zy} = 0.6331$:

$$R_{yz} = \left(\overline{atanh(r_{yzmax})}\right)^{-1} \tag{3}$$

$$r_{yzmax} = max_{u,v\in\{i\}\times\{-n/2,\ldots,n/2\}} C\left(\overline{x,y},u,v\right). \tag{4}$$

Appendix B

B.1 Simulations for elliptical nanoparticle

Complementary to section 3, this appendix presents simulation of an aspherical particle, i.e. an oblate spheroid. An ellipsis with half axes of horizontal $r_1 = r_2 = 0.05$ μm and vertical $r_3 = 0.0125$ μm made of PSL is placed over the surface of a silicon wafer. For the fixed position of the scanning line above the particle at $z = -0.11$ μm, the comparison between the corresponding simulated differential signals is shown in figure B1. The differential signal from the spherical particle has a much larger amplitude compared to the elliptical particle (since the volume of the elliptical particle is four times smaller than for the spherical of the same material). That is why we have normalised the signal so that the shape of the differential signals can be easily observed. For both profiles the maximum and minimum of the differential signal lie in the positions when the particle is at $x = -0.4$ μm and $x = 0.4$ μm, respectively. An important conclusion from figure B1 is that both profiles exhibit asymmetry between the positive and negative lobes of the signal, which is crucial for building the S-curve of the through-focus signal.

Similarly to figure 5, we look at near-field E_z phase distributions above and below the focus, but now with the particle shape set to elliptical (figure B2) Similarly to the figure 5 the phase changes in the Z component are more pronounced than the other polarisation components, both by shifting the ellipsis horizontally and by looking at different z positions, both in magnitude and spatial changes of the phase of the near field. We are interested in the particle positions that correspond to the extrema in the differential profile, such as when $x = -0.4$ μm and $x = 0.4$ μm. Compared to the results in figure 5, the change of particle shape renders a non-negligible effect on the phase distribution. Since the proposed focus-finding technique relies only on the difference between the peaks in the measured signal $|I_{\max}| - |I_{\min}|$ as a function of the Z displacement, non-spherical particles could also be considered in our technique.

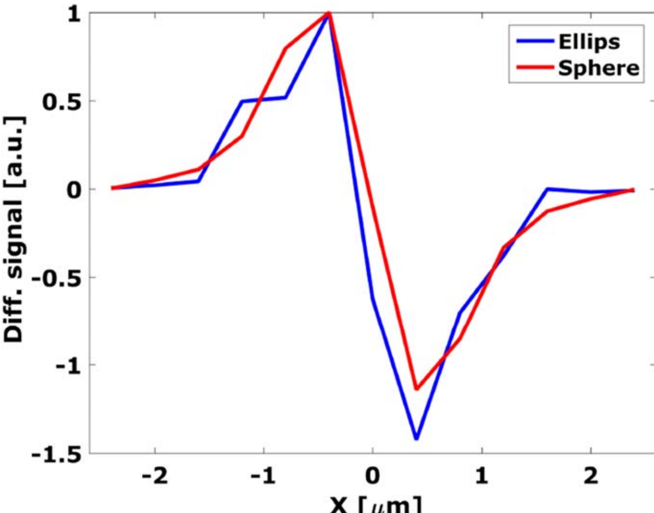

Figure B1. Comparison between the differential signals produced by the sphere (red) and by the ellipsis (blue). Each profile is normalised to unity.

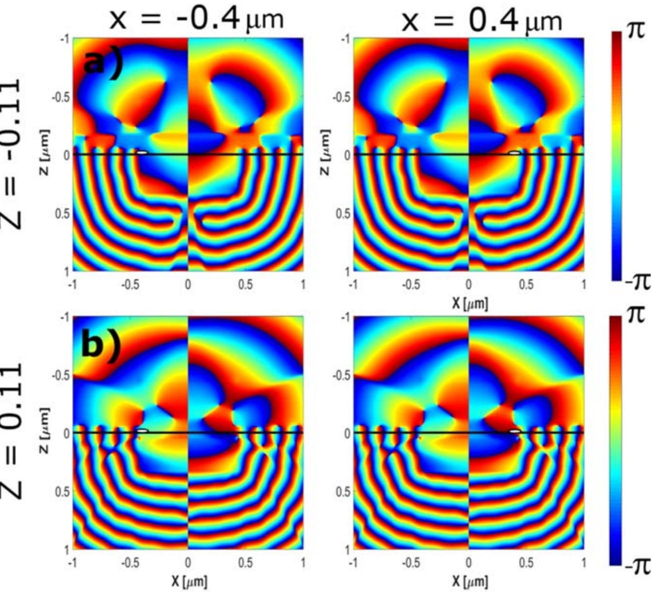

Figure B2. The $E_z$phase distributions in the XZ plane of an elliptical PSL particle $r_1 = r_2 = 0.05$ μm and vertical $r_3 = 0.0125$ μm on top of silicon. The particle is moved in the X direction through the focussed beam centred at $X = 0$. Upper panel: (a) $z = -0.11$ μm. Lower panels: (b) $z = 0.11$ μm. The particle in the X axis is positioned at $x = -0.4$ μm in (a) and (c), and $x = 0.4$ μm in (b) and (d).

ORCID iDs

Dmytro Kolenov https://orcid.org/0000-0003-4205-1925
Peiwen Meng https://orcid.org/0000-0003-2888-5675

References

[1] Liu X 2001 Method and apparatus for determining focus position of a laser *US Patent* 6 303 903 B1
[2] Sevenler D, Oğuzhan A and Ünlü M S 2017 Quantitative interferometric reflectance imaging for the detection and measurement of biological nanoparticles *Biomed. Opt. Express* **8** 2976–89
[3] Mack C A 1993 Understanding focus effects in submicrometer optical lithography: a review *Opt. Eng.* **32** 2350–62
[4] Ilya A *et al* 2017 Determination of laser beam focus position based on secondary speckles pattern analysis *Appl. Opt.* **56** 7413–18
[5] Binh C 2016 *et al* Design and performance of a focus-detection system for use in laser micromachining *Micromachines* **7** 2
[6] Bouwhuis G *et al* 1987 *Principles of Optical Disc Systems* (Bristol: Adam Hilger) pp 70–87
[7] Stout K J and Dong W P 1994 *Three Dimensional Surface Topography: Measurement, Interpretation, and Applications* (London: Penton)
[8] Ingrid S, Steven S S P and Branko P 1990 Effect of focus on cell detection and recognition by the cell analyzer *Cytometry* **11** 460–7
[9] Herbert A D, Carr A M and Hoffmann E 2014 FindFoci: A focus detection algorithm with automated parameter training that closely matches human assignments, reduces human inconsistencies and increases speed of analysis *PLOS One* **9** 1–33
[10] Lindfors K *et al* 2004 Detection and spectroscopy of gold nanoparticles using supercontinuum white light confocal microscopy *Phys. Rev. Lett.* **93** 037401
[11] Trueb J T *et al* 2017 Robust visualization and discrimination of nanoparticles by interferometric imaging *IEEE J. Sel. Topics Quantum Electronics* **23** 9
[12] Ortega-Arroyo J and Kukura P 2012 Interferometric scattering microscopy (iSCAT): new frontiers in ultrafast and ultrasensitive optical microscopy *Phys. Chem. Chem. Phys.* **14**
[13] Ekiz-Kanik F *et al* 2017 Surface chemistry and morphology in single particle optical imaging *Nanophotonics* **6** 713–30
[14] Zhu J *et al* 2019 Regularized pseudo-phase imaging for inspecting and sensing nanoscale features *Opt. Express* **27** 6719–33
[15] Zhu J *et al* 2019 Sensing sub-10 nm wide perturbations in background nanopatterns using optical pseudoelectrodynamics microscopy (OPEM) *Nano Lett.* **19** 5347–55
[16] Webb R H 1996 Confocal optical microscopy *Rep. Prog. Phys.* **59** 427–71
[17] Petra S J H and Gawhary O E 2015 Method and Apparatus for Determining Structure Parameters of Microstructures *Technical Report*
[18] Roy S *et al* 2015 High speed low power optical detection of sub-wavelength scatterer *Rev. Sci. Instrum.* **86** 123111
[19] Mainsah E, Greenwood J A and Chetwynd D G 2001 *Metrology and Properties of Engineering Surfaces (Optoelectronics, Imaging and Sensing Series)* (New York: Springer) pp 87–100
[20] van de Nes A S *et al* 2004 Calculation of the vectorial field distribution in a stratified focal region of a high numerical aperture imaging system *Opt. Express* **12** 1281–93
[21] Marcel L *et al* 2006 Fast focus field calculations *Opt. Express* **23** 11277–91
[22] Farrance I and Frenkel R 2012 Uncertainty of measurement: a review of the rules for calculating uncertainty components through functional relationships *Clin. Biochem. Rev*. **33** 49–75
[23] Ilya A *et al* 2013 Laser focus positioning method with submicrometer accuracy *Appl. Opt*. **52** 415–21
[24] Hwu E-T *et al* 2012 An astigmatic detection system for polymeric cantilever-based sensors *J. Sensors* **2012** 580939
[25] Chiu Y *et al* 2009 Design and fabrication of a small-form-factor optical pickup head *IEEE Trans. Magn.* **45** 2194–2197
[26] Lee Y-C *et al* 2013 A compact optical pickup head in blue wavelength with high horizontal stability for laser thermal lithography *Opt. Express* **21** 23556–67
[27] Sato Y, Noriyuki K, Kawano N, Nishiyama T and Utsonomiya H 2008 Optical head device and optical recording and reading system *US Patent* 8107349B2
[28] Braat J and Török P 2019 Chapter 5 *Imaging Optics* vol **287** (Cambridge: Cambridge University Press) pp 266–378
[29] Bobbert P A and Vlieger J 1986 Light scattering by a sphere on a substrate *Physica* A **137** 209–42
[30] Elton W, Howard R H and Randal K G 1997 Measurement of silicon particles by laser surface scanning and angle-resolved light scattering *Electrochem. Soc* **144** 243–50
[31] Huayao D 2010 Contamination Blog Classification & Analysis on Metallic Contamination in Semi-Conductor Manufacturing Industry (https://blog.associatie.kuleuven.be/danhuayao/)
[32] Park J-E *et al* 2016 Metal nanoparticles for virus detection Jeong-Eun Park, Keunsuk Kim, Yoonjae Jung, Jae-Ho Kim, Prof. Jwa-Min Nam *ChemNanoMat* **2** 927–36
[33] Cacace L A 2009 An optical distance sensor: tilt robust differential confocal measurement with mm range and nm uncertainty *PhD Thesis* Technical University Eindhoven
[34] Joint Committee for Guides in Metrology 2008Evaluation of measurement data—guide to the expression of uncertainty in measurement *Technical Report* (JCGM)
[35] Friedman J H 1984 A variable span smoother *Technical Report* Laboratory for Computational Statistics, Department of Statistics, Stanford University
[36] Daniel C *et al* 2017 Large-field-of-view optical elastography using digital image correlation for biological soft tissue investigation (erratum) *J. Med. Imaging* **4** 029801
[37] Bruck H A *et al* 1989 Digital image correlation using Newton–Raphson method of partial differential correction *Exp. Mech.* **29** 261–7